Lensless Particle Image Velocimetry

Jenna Eppink[1*] and Chung-sheng Yao[1†]

[1*]Flow Physics and Control Branch, NASA Langley Research Center, Hampton, 23681, VA, USA.

*Corresponding author(s). E-mail(s): jenna.eppink@nasa.gov;
Contributing authors: c-s.yao@nasa.gov;
†These authors contributed equally to this work.

Abstract

The application of lensless imaging to particle image velocimetry (PIV) is demonstrated. Lensless PIV eliminates the need for imaging lenses to measure flow fields near a surface. Only the camera sensor, a thin mask, and computations are required to image particles in a flow field and to compute the velocity field. The small form factor could enable embedded sensors for near-wall measurements. Flow field measurements are obtained simultaneously for a lensless system and lens-based 2D PIV system, and several different reconstruction techniques are demonstrated. The reconstructed particle images and computed velocity fields compare well for both a uniform and shear flow. The potential for stereo and 3D volumetric PIV with a single camera sensor is demonstrated through different image reconstruction approaches.

1 Introduction

Particle Image Velocimetry is a well-known and widely used technique (Adrian, 2005) that, in its simplest form, requires the use of a camera, laser (or other focused light source), laser optics, particles, and imaging lens. The lens is used to focus the camera field of view onto the measurement plane of interest, where the thin (≈1 mm) laser sheet defines the measurement location. Seeding particles are injected into the flow, and doubly exposed images are acquired at a short time interval. Typically, a cross-correlation algorithm is performed to extract the quantitative velocity field from the particle displacements. In many cases, when used in a wind tunnel, large magnification is required, either

due to long distances from the windows to the model, or due to the required spatial resolution. Thus, the imaging lens is often the largest component of the imaging system. However, with the emergence of lensless imaging, a lens is no longer required, and the miniaturization of camera sensors can be exploited to allow placement of sensors in locations that would previously have been impossible due to the size of the lens. For instance, sensors could be embedded in the surface of wind tunnel models to allow for near-wall measurements.

Lensless imaging is an optical configuration that replaces the lens of the camera with a thin light-modulating mask and image reconstruction from appropriate computational reconstruction algorithms (Antipa et al, 2018; Boominathan et al, 2022). This allows one to take advantage of the miniaturization of the camera sensor, because the lens is typically the largest component of a camera module. Current applications for lensless imaging include microscopy, wearables and implantables, photography, and in vivo imaging. In addition to the obvious advantage of the small size of the sensor, lensless imagers encode more information than a traditional camera-lens system. This is because the lensless system does not focus the light from a point in the scene to a point on the sensor, but rather it embeds angular information of particle locations. Thus, it is possible to reconstruct a 3D image from a single sensor. Various other methods for single-sensor 3D reconstruction and also lensless concepts for flow field measurements have been used in somewhat limited cases, such as astigmatism PIV, microlens arrays/light-field cameras, and holographic PIV (Cierpka and Kähler, 2012; Hinsch, 2002; Perwass and Wietzke, 2012).

In lensless imaging, the mask, which acts as the encoding element, can be optimized for various applications (Lee et al, 2023). Different types of masks have been demonstrated, including amplitude masks, diffractive masks, diffusers, random reflective surfaces, and modified microlens arrays (Antipa et al, 2018; Kuo et al, 2020). The general idea of lensless imaging is that a point source will create a certain pattern on the camera sensor after passing through the mask, called the point spread function (PSF). If the point source shifts by a given amount, the pattern also shifts a number of pixels that depends on the magnification. If multiple point sources (or particles) are present, the image is basically a sum of all of the PSFs created by the single particles or point sources. Along with an adequate calibration (consisting of one or more measured PSFs), the encoded information on the camera sensor can be used to reconstruct the image. Typically, a forward model is used to represent the relationship between the raw camera image and the scene that is being imaged (Boominathan et al, 2022). Under certain assumptions, such as shift-invariance of the PSF and intensity linearity, a convolutional model can be used, which only requires the acquisition of a single PSF, rather than a PSF for every point in space. This makes the problem much more feasible, however, some of the required assumptions may not hold for the application of lensless imaging to PIV. For example, the linearity assumption may not hold

for a coherent light source, such as a laser. Additionally, the PSF is only shift-invariant locally for small mask-to-sensor distances. In addition to forward models, there is also a growing body of work on using deep learning for lensless image reconstruction (Sinha et al, 2017).

The purpose of this letter is to demonstrate the feasibility and potential advantages of the lensless PIV approach. A simple lensless PIV setup, constructed with readily available and off-the-shelf components, is described. Simultaneous measurements are made with a lens-based 2D PIV setup for verification purposes. Several different image reconstruction techniques are demonstrated, some of which illustrate the potential for stereo or 3D measurements.

2 Methods

2.1 Experiment Setup

The lensless PIV (LLPIV) system consists of a high-speed PIV camera and a thin light-modulating mask (Fig. 1), similar to the setup of Antipa et al (2018). Note that the choice of camera was driven primarily by the ability to place the mask somewhat close to the sensor, and the availability of the equipment. The mask is a thin piece of patterned plastic that acts as a diffuser and creates a focused caustic pattern when placed approximately 9.5 mm from the sensor. The sensor is approximately 25 mm x 16 mm, with 10μm sized pixels, and 2560 x 1600 resolution. A thin ($\approx$ 1 mm) laser sheet, from a 532 nm double-pulsed Nd:YLF laser, is focused approximately 19 mm from the mask. The relative locations of the sensor to the mask, and the mask to the laser plane, determine the magnification of the system. For our current setup, this results in a 1:2 magnification. The lens-based PIV setup, for particle image verification, consists of a time-resolved camera and a 50-mm lens, resulting in a 1:1 magnification of the laser plane. The laser, optics, and camera used for the demonstration are all off-the-shelf components, and the particles are produced using a mini fog machine. The flow field is created using a small open jet wind tunnel. For the acquisition of the PSFs, a broadband LED light source is placed behind a 25 μm pinhole, mounted on a three-axis traverse, and located at the measurement plane. The pinhole and light source are traversed in-plane at 0.5 mm increments across the entire 2D field of view to acquire PSFs at multiple in-plane locations. An example PSF is shown in Fig. 2(a). Several different materials were attempted before choosing the current mask. The performance of the mask was evaluated by the focus and scales of the PSF. The mask is a critical component of the system, since it directly affects the quality and resolution of the reconstruction. There is likely much room for improvement, but for the current demonstration, we choose a functioning mask that is readily available. Scales were applied to the final lensless PIV results by computing the PSF shift that occurred for a translation of 0.5 mm. This shift was found to be 26 pixels and was uniform across the whole field of view. A standard 2D calibration was performed for the lens-based PIV system.

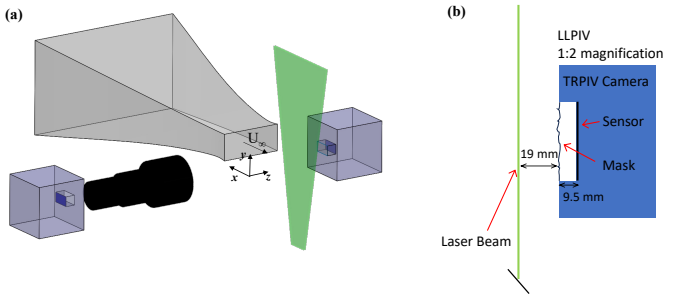

Fig. 1 Schematic of LLPIV verification test setup.

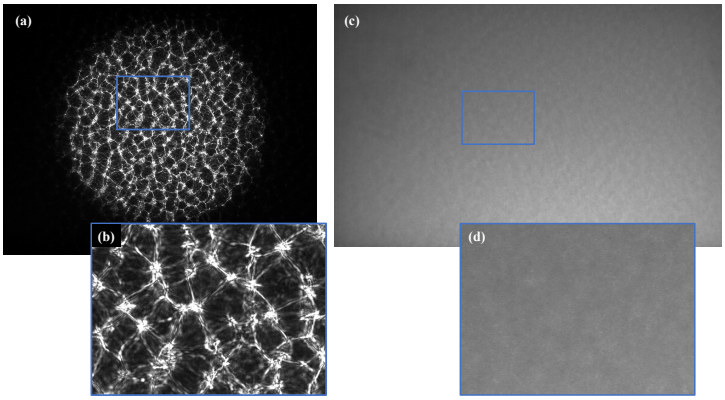

Fig. 2 Example **a-b** PSF and **c-d** raw particle image.

2.2 Data Processing Methods

There are potentially numerous acceptable ways to approach the post-processing for lensless PIV. We describe and demonstrate a few potential approaches in the present work, with the goals of demonstrating the feasibility and highlighting the potential advantages of lensless PIV.

2.2.1 Image Pre-processing and Calibration

Since any background reflections of the laser light can affect the quality of the image reconstruction, we found it necessary to perform some pre-processing of the raw lensless particle image. A POD-based noise removal technique, similar to that introduced by Mendez et al (2017), was successful at removing the background noise and allowed an adequate recovery of the particle image. For the cases shown here, the POD was performed over 300 images, and the image was reconstructed with the first 2-3 POD modes removed, representing backgrounds.

The first step in the reconstruction is to obtain an appropriate calibration. The calibration essentially consists of one, several, or many PSFs, depending on the reconstruction method. The simplest convolutional model only requires

a single PSF at each depth (z) of interest (Antipa et al, 2018), but there are several assumptions required that may not be acceptable in our current application. In particular, we have found that a particle located near the center of the point source that created the PSF used for the deconvolution appears much stronger in the reconstruction than one that is located farther away. This angular sensitivity is observed by (Antipa et al, 2018) as well. Thus, the use of a single PSF may not be adequate to accurately reconstruct the particle image over the entire field of view. The alternative, doing an exhaustive calibration for each camera pixel, is completely infeasible due to the number of PSFs required and the computational resources required to complete the image reconstruction. In addition, our PSF does not cover the entire camera sensor, therefore, multiple PSFs would be required to cover the entire available field of view. Since many deconvolutions are required for the reconstructions noted below, the time required for reconstruction could be a disadvantage for these approaches. The processing time for each deconvolution with 200 iterations was approximately 0.85 seconds on a typical workstation.

2.2.2 Local Vector Approach

To account for these issues, we developed a local vector approach that involves acquiring PSFs with a relatively fine spacing (0.5 mm) across the entire field of view of the camera. We then deconvolve small subsections of the raw lensless image (typically 300x300 pixels) with the local PSF using the Lucy-Richardson deconvolution algorithm. This reconstructs each small subset of the image and allows us to do a local cross-correlation between doubly-exposed image 1 and 2 to build up the vector field for the entire image. Empirically, we found 300x300 pixels to be an optimal size for the reconstruction. Smaller windows resulted in noisier reconstructions, and larger ones required more time to complete the computations but did not significantly enhance the result. An iterative approach with smaller subwindows can then be utilized for the cross-correlation step to improve the spatial resolution, similar to the iterative approach in PIV processing. The main disadvantage of this approach is that the vector-field resolution is limited to the PSF spacing. This means that the calibration can be time-consuming if better resolution is desired, particularly if a 3D calibration is performed. However, the calibration only needs to be performed once. For the current test, we only covered a subsection of the entire sensor: approximately 20 mm x 7 mm, which required 546 PSF images for a single plane.

2.2.3 Overlapping Reconstruction

A variation of the local vector approach is to build up the full particle image by adding up all of the smaller reconstructed windows. Since our window size is 300 x 300 pixels, and a 0.5 mm shift in space corresponds to a PSF shift of 26 pixels, there is significant overlap between adjacent windows. We account for the overlap by performing an average over each reconstructed pixel. This approach allows the noise to be somewhat filtered out because if a particle is present, it will appear in multiple adjacent reconstructed images. Then, the

typical PIV cross-correlation algorithm can be applied to compute the vector field over the full reconstructed particle image. Note that, for 2D PIV, the reconstructed particle image mosaic can be affected by the stereo effect if there is substantial out-of-plane motion of the particles or if the laser plane is not very thin.

2.2.4 Stereo Local Vector Approach

An alternative or variation of the local vector approach, which will allow measurements of out-of-plane motion, is to perform the deconvolution over multiple windows for each PSF, rather than just a window located at the center of the PSF. That is, within each PSF, several interrogation subzones are selected. If the particles are not in the same plane at which the PSF was acquired, there will be a difference between the particle locations when they are processed based on different subzones of the PSF. Similarly, any out-of-plane motion will also produce different vectors when the cross-correlation is performed between the two images. For the current setup, we do not have any substantial out-of-plane motion to measure, nor could it be verified with the 2D lens-based PIV setup. However, we demonstrate the concept using a point source to produce PSFs at varying depths (Fig. 3). The resulting reconstructed particle locations from the left (red) and the right (green) windows for two different depths are shown in the insets of Fig. 3(**b**), and the profiles across the middle of the particles are shown in the plot. The minimum resolvable distance will be determined by the magnification of the system, the separation of the two windows that are measured (in our case 400 pixels), as well as the properties of the mask. For the current case, a shift of approximately 1 pixel is observed for an axial distance of 0.2 mm, and the shift is approximately 4 pixels for Δz =0.6 mm. There is also a clear degradation of the signal of the reconstructed particles as the axial distance is increased. Thus, this technique would be limited to small axial distances, which would work well for a typical stereo PIV setup in which the laser sheet is typically on the order of 1 mm thick.

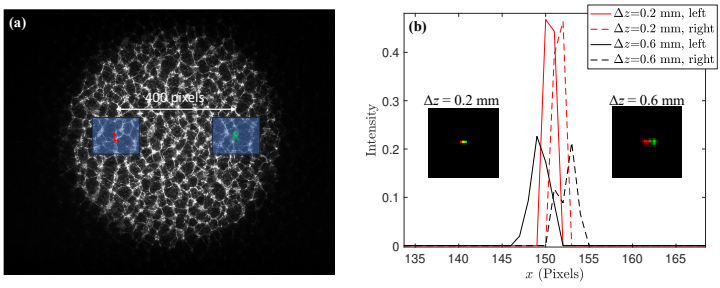

Fig. 3 **a** Sketch of stereo PSF processing subzones. **b** Example reconstructed particles from pinhole images taken at varying depths (insets) and the intensity profiles across the middle of the particles.

2.2.5 3D Reconstruction

Finally, we demonstrate the 3D capability of lensless imaging on a particle image using the approach of Antipa et al (2018). This technique relies on the assumptions mentioned previously that allow the use of a single PSF at each depth. Their algorithm uses the alternating direction method of multipliers (ADMM) to reduce the computational time required to solve the large inverse problem. This method also incorporates a sparsity parameter, which allows the user to control the level of sparsity of the reconstruction. A sparsity-constrained optimization could be ideal for particle image reconstruction, which is sparse by nature. However, this has not been studied in detail for the current work. For the calibration, a PSF is required at multiple depths throughout the field of interest. We acquired 49 PSFs with an axial spacing of $\Delta z = 0.2$ mm located at the center of the field of view.

3 Results

3.1 2D Results

An example reconstructed particle image using the overlapping reconstruction approach is shown in Fig. 4. The particles reconstructed from the lensless image are shown in black, while the lens-based PIV particle image is shown in red. The lensless image was scaled and shifted to align with the PIV image. The images are purposefully offset slightly to allow for easier comparison (LLPIV to the left). Many of the particles that are visible in the PIV particle image are also visible in the LLPIV reconstructed image, although there are a number of particles that were also not seen by the LLPIV system. This could be due to several factors, one of which is the difference in magnification between the two systems. The other potential issue mentioned previously is the stereo effect that could be negatively impacting the reconstruction. Regardless, this is an encouraging result since we can clearly verify that the particles imaged by the LLPIV system are the same particles seen by the lens-based PIV system. It should be noted that the seeding density is relatively low, even in the lens-based PIV images. We estimate a particle density of approximately 4-5 particles per 64x64 pixel interrogation window. The lensless system achieved approximately 60% of that particle density, on average. Maintaining consistent and dispersed seeding was difficult with the current setup. In addition, if the particle seeding was too dense, the lensless sensor would saturate. Thus, there may be a limit to how many particles can be imaged for a given lensless setup.

Flow field data were acquired first for a uniform flow field. The time-averaged results over 200 images are shown in Fig. 5. LLPIV results are shown for both the overlapping reconstruction method (5(a)), and the local vector method (5(b)). In order to quantify the difference in measured velocity across the field of view, the time-averaged PIV velocity is first interpolated onto the LLPIV grid, and then the difference is computed ($\Delta U = \overline{U}_{LLPIV} - \overline{U}_{PIV}$). For the most part, the LLPIV results are within 3% of the PIV results for both

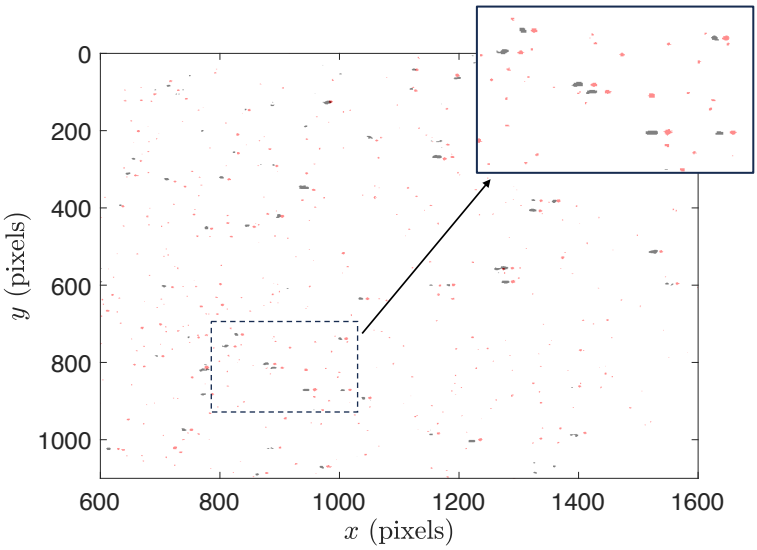

Fig. 4 Comparison of a reconstructed (inverted) particle image from the lensless camera (black) and the particle image from the lens-based PIV setup (red)

reconstruction methods. A more extensive calibration of the LLPIV camera would likely improve the comparison. Additionally, the u'_{rms} results are computed by taking the root mean square of the differences at each location over each of the 200 instantaneous flow fields. These values mainly fall within 4 to 10%. The differences are larger near the left and right edges of the field of view (>10%). This area tended to have less particle density because it is near the edge of the laser sheet. One problem with the LLPIV approach, as currently implemented, is that there can be some noise present in the reconstructed image, particularly in areas where no or very few particles are present. Thus, in some cases, spurious vectors are sometimes computed in regions with low particle density.

To increase the complexity of the flow, and to get an idea of how well the LLPIV technique works in flows with gradients, the wind tunnel was elevated so that the cameras were imaging the shear layer coming from the bottom of the wind tunnel exit. An example comparison between the processed flow fields is shown in Fig. 6. Only the overlapping reconstruction method results are shown here, due to the limited area coverage and resolution of the local vector field approach. Similar flow structures are seen in the U-velocity fields, and the vectors agree well. However, once again there is more noticeable disagreement near the left edge of the measurement region. Overall, the results are very encouraging for a first attempt at this technique.

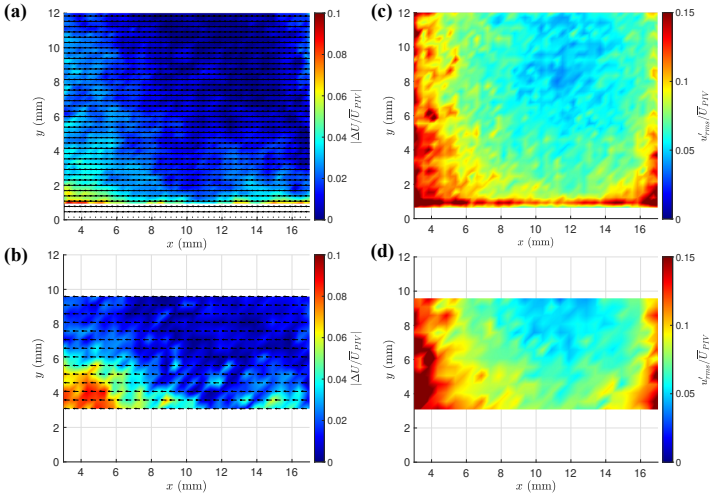

Fig. 5 Example processed PIV results for a uniform flow field, in which the flow is from right to left. The time-averaged LLPIV vector field is overlaid on contours of the normalized difference in mean U velocity for the **a** Overlapping Reconstruction Method and **b** Local Vector Method. Contours of the normalized u'_{rms} velocity are shown for the **c** Overlapping Reconstruction Method and **d** Local Vector Method.

3.2 3D Results

Results for the 3D reconstruction are shown in Fig. 7. In Fig. 7(**a**), the 3D reconstruction is compared with the 2D reconstruction of the same particle image in the $x - y$ plane. The 3D result actually consists of multiple reconstructed planes (one for each PSF provided in the calibration), so for comparison purposes, the intensity is summed up over a z-depth of 2 mm in order to capture all the particles in the laser plane. A slight offset is included to allow for ease of comparison. Many of the same particles are recovered by the 3D reconstruction, but several, particularly near the top and left side, are not. This could be due to the fact that we use a single PSF per plane for the 3D reconstruction.

Due to the relatively thin laser plane, the 3D capability is demonstrated by taking separate particle images with the laser plane translated by 0.5 mm between the two images. This result is shown in Fig. 7(**b**). The intensities are shown in red and black for the two separate laser planes. A clear shift is evident between the two images, corresponding to approximately 0.5 mm in z, although there is some overlap between the two as the laser plane appears to have a thickness of approximately 1.5 mm. This 3D reconstruction capability demonstrates the potential for doing volumetric PIV measurements with a single camera sensor, although more work needs to be done to determine how well the system can resolve out-of-plane motion of the particles.

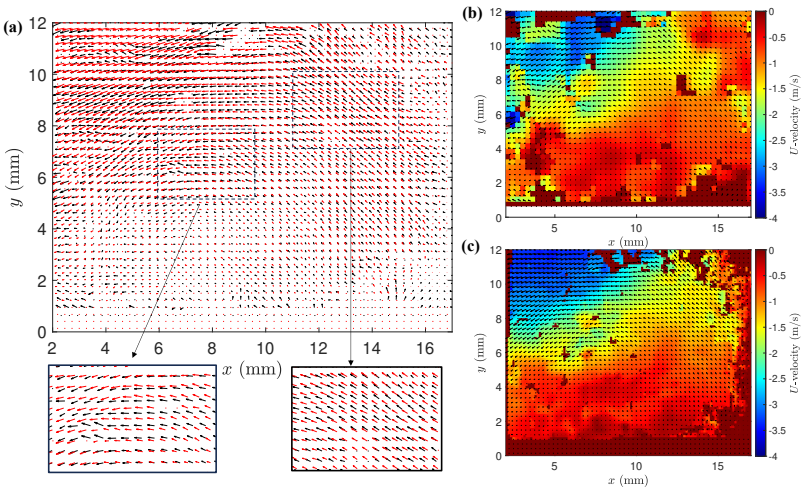

Fig. 6 Example processed instantaneous PIV results for the shear layer. **a** Vector field comparison with LLPIV (black) and lens-based PIV (red), with zoomed-in views below. Vector fields overlaid on U-velocity contours from the **b** LLPIV measurements and **c** lens-based PIV measurements

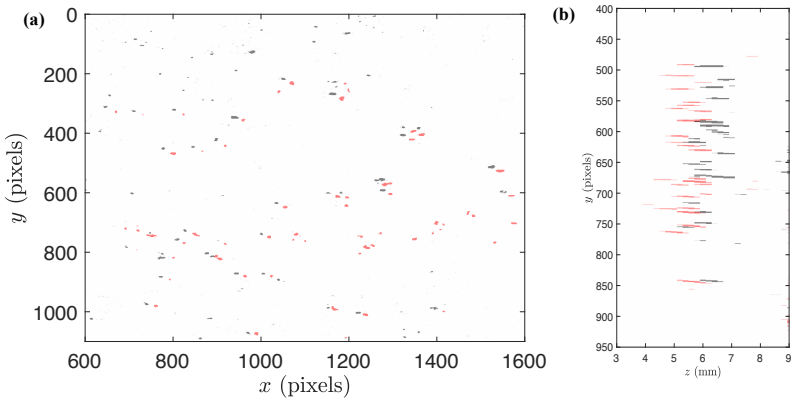

Fig. 7 **a** Comparison between 2D (black) and 3D (red) reconstructed particles. For the 3D reconstruction, intensities are summed over a z-range of 2 mm. **b** Comparison between particle images taken with the laser plane at two different z-depths, separated by 0.5 mm. Intensities are summed in x.

4 Conclusions

Lensless particle image velocimetry was demonstrated for the first time using a simple setup with readily available and off-the-shelf PIV equipment. The velocity measurements were compared with measurements made using a lens-based 2D PIV setup. The particle images and velocity field results agreed well with the PIV results, though there is plenty of room for improvement. Several areas, such as the design of the mask, reconstruction and post-processing

algorithms, and other system parameters need to be studied and optimized. The main advantages of the lensless PIV system are its potentially small size and its three-dimensional capability, along with the flexibility and versatility of the system. The LLPIV system could conceivably be embedded in a model surface, allowing near-surface velocity measurements that would otherwise be impossible for some applications. Additionally, the stereo and 3D capabilities of lensless imaging open the potential for 3D flowfield measurements with only a single sensor, in a simple, compact, system.

Declarations

Ethical Approval

This declaration is not applicable.

Competing Interests

The authors declare they have no competing interests to disclose.

Authors' Contributions

Both authors contributed equally to the conceptualization and implementation of the idea. J.E. prepared the manuscript, and all authors reviewed the manuscript.

Funding

The authors declare they have no funding to disclose.

Availability of data and materials

The data may be made available upon request to the corresponding author.

References

Adrian RJ (2005) Twenty years of particle image velocimetry. Experiments in fluids 39:159–169

Antipa N, Kuo G, Heckel R, et al (2018) Diffusercam: lensless single-exposure 3d imaging. Optica 5(1):1–9

Boominathan V, Robinson JT, Waller L, et al (2022) Recent advances in lensless imaging. Optica 9(1):1–16

Cierpka C, Kähler CJ (2012) Particle imaging techniques for volumetric three-component (3d3c) velocity measurements in microfluidics. Journal of visualization 15:1–31

Hinsch KD (2002) Holographic particle image velocimetry. Measurement Science and Technology 13(7):R61

Kuo G, Liu FL, Grossrubatscher I, et al (2020) On-chip fluorescence microscopy with a random microlens diffuser. Optics express 28(6):8384–8399

Lee KC, Bae J, Baek N, et al (2023) Design and single-shot fabrication of lensless cameras with arbitrary point spread functions. Optica 10(1):72–80

Mendez M, Raiola M, Masullo A, et al (2017) Pod-based background removal for particle image velocimetry. Experimental Thermal and Fluid Science 80:181–192

Perwass C, Wietzke L (2012) Single lens 3d-camera with extended depth-of-field. In: Human vision and electronic imaging XVII, SPIE, pp 45–59

Sinha A, Lee J, Li S, et al (2017) Lensless computational imaging through deep learning. Optica 4(9):1117–1125